



Open Research Online

Citation

Al-Rashdi, K. S.; Elzain, M. E.; Al-Barwani, M. S.; Moore, E. A. and Widatallah, H. M. (2023). Computational modeling of the defect structure, hyperfine and magnetic properties of the Mn²⁺-doped magnetite of the composition Mn Fe₃O₄ ($y = \frac{2}{3} x$). Materials Research Bulletin, 159, article no. 112095.

URL

<https://oro.open.ac.uk/85961/>

License

(CC-BY-NC-ND 4.0) Creative Commons: Attribution-Noncommercial-No Derivative Works 4.0

<https://creativecommons.org/licenses/by-nc-nd/4.0/>

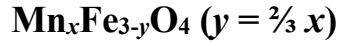
Policy

This document has been downloaded from Open Research Online, The Open University's repository of research publications. This version is being made available in accordance with Open Research Online policies available from [Open Research Online \(ORO\) Policies](#)

Versions

If this document is identified as the Author Accepted Manuscript it is the version after peer review but before type setting, copy editing or publisher branding

Computational modeling of the defect structure, hyperfine and magnetic properties of the Mn²⁺-doped magnetite of the composition



K. S. Al-Rashdi¹, M. E. Elzain¹, M. S. Al-Barwani², E. A. Moore³, H. M. Widatallah^{1,*}

¹*Department of Physics, College of Science, Sultan Qaboos University, P. o. Box 36, Al-Khoudh, Muscat 123, Oman*

²*Center for Research Computing, NYU Abu Dhabi, P.O. Box 129188, Saadiyat Campus, Abu Dhabi, United Arab Emirates*

³*Department of Life, Health and Chemical Sciences, The Open University, Walton Hall, Milton Keynes, MK7 6AA, UK*

*hishammw@squ.edu.om

Abstract

The defect structure, hyperfine and magnetic properties of Mn²⁺-doped Fe₃O₄, where Mn²⁺ substitutes for Fe³⁺ to yield Mn_xFe_{3-y}O₄ ($y = \frac{2}{3}x$), have been modeled using atomistic and DFT calculations. Atomistic simulations show the substitution of Mn²⁺ for Fe³⁺ at the tetrahedral sites to be energetically more favorable relative to its substitution at octahedral sites. Such substitutions of Mn²⁺ impurities are balanced by the occupation of either Mn²⁺ or Fe³⁺ cations for interstitial sites. GGA with on-site Coulomb interaction approximations (GGA+U) for the exchange-correlation potential were used to calculate the electronic structure and discuss the hyperfine and magnetic properties of the structurally most preferred models of Mn_xFe_{3-y}O₄. A comparison of the results obtained shows that the model in which all Mn²⁺ cations substitute for Fe³⁺ at the tetrahedral sub-lattice, balanced by the expulsion of the Fe³⁺ cations to interstitial sites, is in good agreement with the experimental magnetic and Mössbauer spectroscopic trends.

Keywords: *Magnetite; Defects, Hyperfine; Magnetic Properties, DFT calculations*

1. Introduction

Attractive properties such as high saturation magnetization, **high** Curie temperature and relatively **low room temperature electric** resistance render magnetite (Fe₃O₄) a **functional material in a host of applications that include** ferrofluids, **magnetic storage devices** and **electromagnets**, among others [1-5]. Owing to its biocompatibility, Fe₃O₄ is also useful, in the form of nanoparticles, in several medical applications such as contrast agents in magnetic resonance imaging (MRI) and drug delivery [6-9]. Stoichiometric Fe₃O₄ crystallizes, at ambient conditions, in an inverse-spinel related structure and is often represented by the compositional

formula $(\text{Fe}^{3+})_A[\text{Fe}^{2+},\text{Fe}^{3+}]_B\text{O}_4$, where the round and square brackets refer, respectively, to the tetrahedral (A), and octahedral (B) sites that are randomly occupied by Fe^{2+} and Fe^{3+} ions [6,10,11]. The net saturation magnetic moment of this ferrimagnetic material is given by $M_s = |M_B - M_A|$, where M_A and M_B are, respectively, the magnetic moments of the A- and B-sublattices. The relatively large electrical conductivity of the material ($\sim 250 \Omega^{-1} \text{ cm}^{-1}$) at 300 K, which is comparable to that of a poor metal [12], is attributed to fast electron hopping between the Fe^{3+} and Fe^{2+} ions **at the B-sites** [12,13]. At the so-called Verwey temperature T_V ($\sim 120 \text{ K}$), Fe_3O_4 experiences a first order metal-insulator transition from a cubic cell ($a = 8.3963 \text{ \AA}$) to a lower symmetry crystal structure with an ordered arrangement of the Fe^{2+} and Fe^{3+} ions at the B-sites [6,12-14]. **At T_V** a sharp increase of the material's resistivity by two orders of magnitude [12,15] is noticed **with** the magnetization **changing** abruptly [12,16,17]. Non-stoichiometry that results from cationic substitution or partial oxidation of Fe^{2+} can **lower T_V** or suppress it entirely [15,18]. Early experimental studies proposed two monoclinic (space groups $P2/c$ and Cc) and two orthorhombic (space groups $Pmca$ and $Pmc2_1$) structures for **the material at low temperature** ($<T_V$) [13,19-22]. A theoretical study on optimizing the fully relaxed cells of the low temperature phases by Jeng *et al* showed that while each **phase** could be considered a ground state structure of Fe_3O_4 , the monoclinic Cc cell **has** the lowest total energy [13].

To modify the physical properties of Fe_3O_4 **so as** to suit a wider range of applications, several workers have investigated the effect of cationic impurities on the structural, magnetic and electric properties of the material [2,6,8-10,23]. It has been shown that the site preference of the dopant cations is generally sensitive to the ionic radii mismatch, the formation temperature, **the** coordination preference and **the** electronic configuration [24,25]. In most of these studies, divalent cations (M^{2+}) and trivalent ones were purposely introduced to substitute for Fe^{2+} and Fe^{3+} , respectively, so as to form compounds of the composition $M_x\text{Fe}_{3-x}\text{O}_4$ [2,23,26-28]. Recently we have reported that substituting of Fe^{3+} in Fe_3O_4 by Mn^{2+} to form $\text{Mn}_x\text{Fe}_{3-y}\text{O}_4$ (where $y = \frac{2}{3}x$) nanoparticles leads to formation of defect structures with both substitutional and interstitial Mn^{2+} impurities in contrast to $\text{Mn}_x\text{Fe}_{3-x}\text{O}_4$ where only Mn^{2+} substitutional impurities exist. Our Mössbauer measurements suggest that the cationic distributions in $\text{Mn}_x\text{Fe}_{3-y}\text{O}_4$ ($y = \frac{2}{3}x$) are such that for $x \leq 0.2$ the dopant Mn^{2+} ions substitute **solely** for Fe^{3+} at the A-sites, whereas for $x > 0.2$ they substitute for Fe^{3+} at **the** A- and B-sites [29]. It is, thus, of interest to see whether this defect

structure is the energetically most favourable and how **could it** be correlated with the observed structural, magnetic and electronic properties **of the solid**.

Computational methods are important in modeling the structure and physical properties of solids **and** becoming increasingly valuable complements to experimental and theoretical studies [30,31]. Of these methods, atomistic simulations have been successfully used to optimize the structures of iron oxides, including the distribution of point defects in cation-doped systems by minimizing the lattice energy [32-36]. It has also been shown that conflicting defect structure models for cation-doped iron oxides inferred from experimental data could be unambiguously resolved by combining atomistic simulation and *ab initio* DFT calculations [36,39]. **To our knowledge, there is only one published atomistic simulation study on the defect structure of Sn⁴⁺/Ti⁴⁺ doped Fe₃O₄ [40]. Among the many reported DFT studies on Fe₃O₄ [for example 13,19-22], only few are devoted to the effect of doping on the magnetic and hyperfine properties of the solid [43,44]. In the present work, we report on carrying out a computational modeling study on the effect of Mn²⁺-doping of Fe₃O₄ to form Mn_xFe_{3-y}O₄ ($y = \frac{2}{3}x$). Specifically we report on performing atomistic simulation and DFT calculations to investigate the possible defect and electronic structures of Mn_xFe_{3-y}O₄ ($y = \frac{2}{3}x$) and calculate the associated hyperfine and magnetic properties of the material.**

2. Simulation methods

2.1. Atomistic simulations

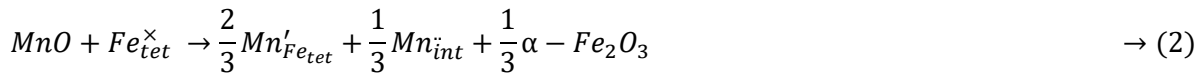
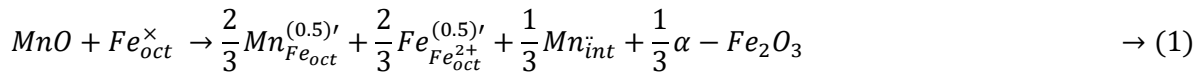
Energies for the possible defect models induced by the incorporation of Mn²⁺ into Fe₃O₄ to form Mn_xFe_{3-y}O₄ (where $y = \frac{2}{3}x$) were calculated using the GULP code [46]. **The following Buckingham pair potential representing the short-range Pauli repulsion, the leading term of any dispersion energy and the Coulomb interaction was used for the inter-atomic potential calculations [47].**

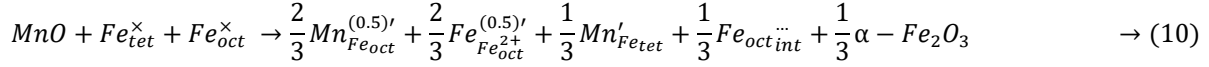
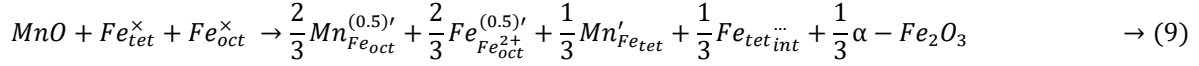
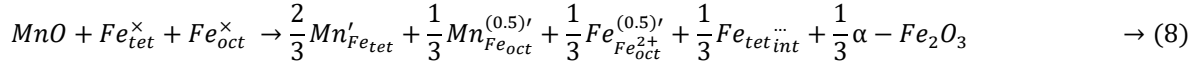
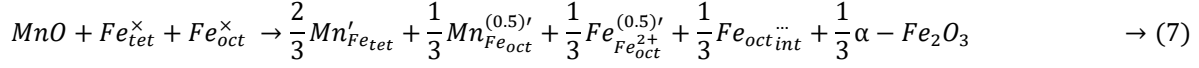
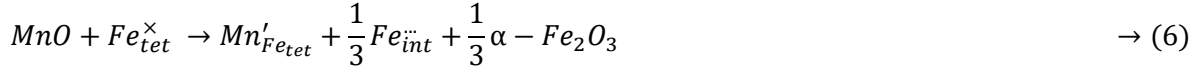
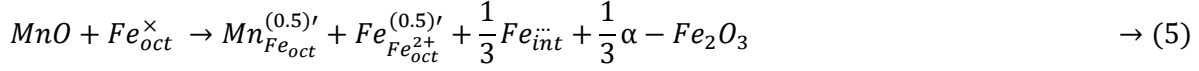
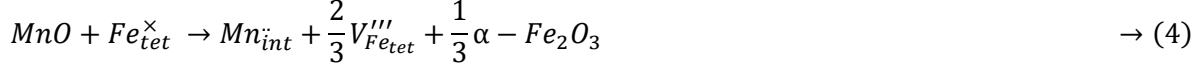
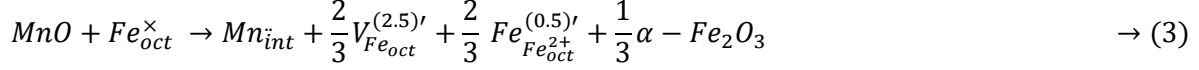
$$V_{ij} = q_i q_j / r_{ij} + A \exp(-r_{ij}/\rho) - C r_{ij}^{-6}$$

where q_i and q_j are the ionic charges, r_{ij} is the inter-ionic spacing and A , ρ and C are constants to be found empirically. The shell model was used for the electronic polarizability of the ions [48]. The interatomic potential parameters, listed in Table 1, used for Fe³⁺, Fe²⁺, Mn²⁺ and O²⁻ were taken from a study of intrinsic defects in Fe₃O₄ (Lewis 1985c library) [49]. The Mott–Littleton approach was used for point defect calculations with the crystal surrounding the defect

being divided into three spherical regions [46-48]. In the first region, the ions were allowed to relax their positions in response to the defect. In the second region, the response of the displaced individual ions to the electrostatic force of the defect was approximated by ions in a harmonic potential well. In the third region, polarization of sub-lattices was only considered [46-48]. The radii of the first and the second regions were set at 8 and 16 Å, respectively. **Care was taken to make sure that the defect energies obtained sufficiently converged with respect to the region radii chosen.**

To rationalize the defect structure that forms when Mn^{2+} is introduced as an impurity defect in Fe_3O_4 , a cubic cell ($Fd\bar{3}m$ # 227) was employed as a starting model with equal occupancy of Fe^{2+} and Fe^{3+} on the octahedral sites to model the average field experienced by the ions. **Here we did calculations for the structure adopted at room temperature to understand the behaviour of the materials under normal condition. It was assumed that the structural transformation of Fe_3O_4 from the disordered cubic cell ($Fd\bar{3}m$) to the ordered low symmetry cell, when the temperature is reduced to 0 K, does not affect the defect structure.** After initially optimizing the unit cell of Fe_3O_4 using a constant pressure energy minimizing scheme, the optimized cell was used to test various defect reaction models for the incorporation of Mn^{2+} into Fe_3O_4 using an approach proposed by Moore *et al* to determine the defect structures of doped spinel-related iron oxides [40]. Delocalized models with Fe^{2+} and Fe^{3+} ions occupying equivalent octahedral sites in disordered fashion that match the composition in which three Mn^{2+} ions substitute solely for two Fe^{3+} ions were considered. In a defect reaction model proposed both mass and charge were considered by balancing the defect through the introduction of either cationic and anionic vacancies or interstitial and substitutional impurities. The essence of this model is that any loss of the Fe^{3+} ion from an octahedral site is assumed to leave another octahedral site occupied by Fe^{2+} ion to account for the overall crystal charge balance. This is expressed using the Kröger-Vink notation by the term $Fe_{Fe_{oct}^{2+}}^{(0.5)'}$ in the defect models. Cases for simultaneous substitution of Mn^{2+} for Fe^{3+} at both octahedral and tetrahedral sites were also considered. Based on the above, the following defect reaction models were studied.





2.2. Density Functional Theory (DFT) calculations

Electronic calculations were performed within the framework of density functional theory method using the full potential linear augmented plane wave (FP-LAPW) scheme as implemented in **the** WIEN2k package [50]. A $1 \times 1 \times 2$ supercell of Fe_3O_4 with $a = b = 5.87126 \text{ \AA}$, $c = 33.16681 \text{ \AA}$, $\alpha = 90.0^\circ$, $\beta = 90.2363^\circ$ and $\gamma = 90.0^\circ$, which was generated using the GULP code as shown in Figure 1, is used as the starting geometry of the material. In constructing the supercell, we started with a fully relaxed monoclinic cell ($P2/c$) with lattice parameters given by $\frac{a}{\sqrt{2}} \times \frac{a}{\sqrt{2}} \times 2a$, and cation distribution among the A- and B-sublattices as acquired from the early reported electronic structural studies of Fe_3O_4 [13,19-21,51,52]. We note that this supercell consists of 112 atoms, which is twice the number of atoms used in previous DFT studies on spinel-based compounds [53]. DFT calculations were carried out for both the pure Fe_3O_4 and the Mn^{2+} doped Fe_3O_4 using the two best defect models attained from atomistic simulations, without performing any optimization for the cell parameters. The Muffin Tin (MT) radii used for Fe and O were 1.85 and 1.59 *au*, respectively, in the case of the pure Fe_3O_4 supercell and 1.39, 1.19, 1.67 *au* for Fe, O, and Mn respectively, in the case of Mn-doped Fe_3O_4 . The generalized gradient approximation plus on-site Coulomb interaction (GGA+U) was used to solve the Kohn-Sham equations. Spin polarization

was used too for the demonstration of ferrimagnetic behavior of the material. The calculations were performed with $6 \times 6 \times 2$ Monkhorst-Pack k-point grid in the Brillouin zone and 75600 plane waves with the cut-off energy of 9.0 Ry (= 122.45 eV). The on-site Coulomb energies, U, used are U = 0.56 Ry (7.62 eV), 0.45 Ry (6.12 eV) and 0.56 Ry (7.62 eV) respectively for Fe³⁺, Fe²⁺ and Mn²⁺. Self-consistent calculations were performed with Energy precision of 5×10^{-7} Ry, and successive charge density ratios of 1×10^{-6} .

3. Results and Discussion

3.1. Atomistic simulation of the defect structure in $Mn_xFe_{3-y}O_4$ ($y = \frac{2}{3}x$):

The calculated point defect and lattice energies for each term in the above defect reactions are listed in Table 2. Calculations of the defect energy of certain terms such as $Mn_{Fe_{oct}}^{(0.5)'}$, are not direct and require the addition or subtraction of other defect energies. The calculated energy obtained for each of the above defect models is listed in Table 3. Substitution of the Mn²⁺ impurities for the octahedral Fe³⁺, such as in model 9a and 9b, is clearly not favourable. The substitution of Mn²⁺ for Fe³⁺ at both tetrahedral and octahedral sites, such as in reactions 7 and 8, is slightly more favourable than case in which the Mn²⁺ ions solely occupy the interstitial sites, such as in reactions 3 and 4. The energetically most favourable defect models involve the substitution of Mn²⁺ ions for tetrahedral Fe³⁺ namely models 2 and 6. The third Mn²⁺ ions, required for charge balance, is apparently decisive in determining which defect structural model is the most stable. In model 2, where this Mn²⁺ ion occupies an interstitial site, the total energy is slightly less than that of model 6 where it substitutes for a tetrahedral Fe³⁺ ion that, in turn, is expelled to an interstitial site. In both models, the occupation of the Mn²⁺/Fe³⁺ ions for interstitial octahedral sites (as in reactions 2b and 6b) is energetically more likely than their occupation for interstitial tetrahedral sites (as in reactions 2a and 6a). These results are consistent with the experimental cationic distribution derived from the XRD data [45]. It is also consistent with crystal field arguments that Fe²⁺ would preferentially occupy octahedral sites whereas Mn²⁺ and Fe³⁺, being d⁵ ions, would have 0 CFSE at both sites [54]. The spatial defect distribution was derived by optimizing a $2 \times 2 \times 2$ supercell of $Mn_xFe_{3-y}O_4$ ($y = \frac{2}{3}x$), where groups of 3 Mn²⁺ ions are introduced instead of groups of 2 Fe³⁺ ions. The results suggest that the impurity Mn²⁺ ions prefer to cluster at adjacent sites rather than being significantly separated from each other as illustrated in Figure 2. Energy minimization has shown these defect clusters to be randomly distributed over the supercell.

To find out which of the above proposed defect models is most likely, a supercell of $\text{Mn}_x\text{Fe}_{3-y}\text{O}_4$ ($y = \frac{2}{3}x$) based on each model was used as input structure for DFT calculations for the Mössbauer parameters and magnetic properties. Then the results were compared to experimental findings.

3.2. The Electronic, Hyperfine and Magnetic properties of Fe_3O_4 :

To appreciate the effect of Mn^{2+} doping on Fe_3O_4 and find out which of the two most favourable defect structure models, derived from atomistic simulations, yields results that are consistent with experimental observations, the electronic properties of stoichiometric Fe_3O_4 were first obtained and compared with those published previously using DFT-based methods [19-21,52]. Figure 3 shows the total density of states (TDOS) calculated for the $1 \times 1 \times 2$ Fe_3O_4 monoclinic supercell using the GGA+ U approximation. The dotted line represents the Fermi level and the asymmetry of the spin-up and spin-down states in the TDOS reflect the ferrimagnetic nature of the solid. The band gap, $E_g \sim 0.78$ eV, is consistent with those reported for the low temperature monoclinic as well as the high temperature cubic Fe_3O_4 , where E_g for the monoclinic cell increases with increasing U reaching 0.63 eV for a U value of 5.5 eV [13]. The obtained E_g width is consistent with calculated results [13,52] but larger than the experimentally reported value (~ 0.14 eV) [22,52]. This may reflect the effect of the U value used in the calculations. The individual contributions of $\text{Fe}^{3+}(\text{A})$, $\text{Fe}^{2+}(\text{B})$, and $\text{Fe}^{3+}(\text{B})$ to the TDOS are shown in Figure 4. Based on the crystal field theory in the mixed valence Fe_3O_4 , with Fe^{3+} ($3d^5$) and Fe^{2+} ($3d^6$) ions, the electronic configuration for the tetrahedral (A) symmetry is $e^2t_2^3$ ($S = \frac{5}{2}$) for Fe^{3+} , whereas those for the octahedral (B) ones of Fe^{3+} and Fe^{2+} are $t_{2g}^3e_g^2$ ($S = \frac{5}{2}$) and $t_{2g}^4e_g^2$ ($S = 2$), respectively [54]. In line with the generally used notation [13,19,20,52] in Figure 1 we label the B-site electron-poor and electron-rich ions, respectively, as $\text{Fe}^{3+}(\text{B}_2/\text{B}_3)$ and $\text{Fe}^{2+}(\text{B}_1/\text{B}_4)$ whereas the A-site ion is labeled as $\text{Fe}^{3+}(\text{A})$. The spin orientation of the majority and minority electrons in the B-site Fe ions (Figure 4,) were chosen to be up and down, respectively. The reverse case is correct for the electrons at the A-sites. The spin-down states, near the Fermi level (~ -0.5 – 0.0 eV), are mainly a contribution of the $3d\text{-Fe}^{2+}(\text{B}_1/\text{B}_4)$ ions that are ascribed to the localized t_{2g} minority charge indicating an orbital ordering in which the t_{2g} spin-down states of Fe^{2+} ions are occupied while those of Fe^{3+} are not [51,52]. In general, the agreement of the above results for Fe_3O_4 with previous

DFT calculations [13,19,20,39] supports the adequacy of using the GGA+*U* approach for the Mn²⁺-doped Fe₃O₄ electronic structure calculations. Additionally, we summarize in Table 4 the calculated hyperfine parameters and magnetic moments at certain Fe sites in the 1×1×2 Fe₃O₄ supercell. The charge density within the MT spheres results in isomer shifts (δ) with larger values for Fe²⁺(B) when compared to the corresponding ones for Fe³⁺(B) ions concurring with the reported Mössbauer data of Fe₃O₄ [29]. The non-zero values of the quadrupole shift (Δ) obtained at the Fe²⁺(B) sites indicate an enhanced asymmetry which, in turn, demonstrates the lower symmetry of the monoclinic Fe₃O₄ cell relative to the experimentally studied cubic one [29]. The magnetic hyperfine field (B_{hf}) at the Fe²⁺(B) sites converges to smaller values than those at the Fe³⁺(A)/ Fe³⁺(B) sites in agreement with the calculated values of the magnetic moments (μ_{Fe}) at these sites. The magnetic moments (μ_{Fe}) at the Fe sites (Table 4), whose directions are indicated with their signs, reveal the high-spin state for Fe³⁺ and Fe²⁺ ions where both t_{2g} and e_g manifolds are populated. **The total magnetic moment per Fe₃O₄ formula unit (f.u.) converges to $4\mu_B$.** Overall, these results show similar trends to the hyperfine parameters and magnetic moments that were measured experimentally for bulk and microcrystalline Fe₃O₄.

3.3. The Electronic, Hyperfine and Magnetic properties of $Mn_xFe_{3-y}O_4$ ($y = \frac{2}{3}x$):

The 1×1×2 supercell of $Mn_xFe_{3-y}O_4$ ($y = \frac{2}{3}x$) resulted in a compositional formula of $Mn_3Fe_{46}O_{64}$. Defining the dopant concentration as the number of Mn²⁺ ions relative to the total number of cations, this formula corresponds to 6% Mn²⁺ doped Fe₃O₄ and matches the $Mn_xFe_{3-y}O_4$ sample with $x = 0.1$ for which we reported the ⁵⁷Fe Mössbauer hyperfine properties [29].

The TDOS for the 1×1×2 $Mn_xFe_{3-y}O_4$ supercell with Mn²⁺ ions substituting for tetrahedral Fe³⁺ ones and the extra Mn²⁺ ions occupying interstitial tetrahedral sites (defect model 2a), shown in Figure 5, reveals the formation of a ferrimagnetic insulator with a reduced band gap of ~ 0.44 eV compared to that of Fe₃O₄. The states in the region near the Fermi-level ($-2 - 0$ eV) originate from the interstitial Mn²⁺ ion as it is clear from Figure 6 which shows the contributions of individual cations to the TDOS. This is to be contrasted with the half-metallic ferrimagnetic behaviour revealed by the calculated TDOS for the 1×1×2 supercell of $Mn_xFe_{3-y}O_4$ with Mn²⁺ ions substituting for tetrahedral Fe³⁺ ones and the extra Mn²⁺ ions substituting for tetrahedral Fe³⁺ ions that are expelled to interstitial tetrahedral sites (defect model 6a) as shown in Figure 7. The gap, that forms in Fe₃O₄ is filled with electronic states associated with Fe³⁺ at the B₃ and interstitial

sites as it is evidently clear from the partial density of states shown in Figure 8. As the electronic configuration for the A-site symmetry Mn^{2+} is $e^2t_2^3$ ($S = \frac{5}{2}$), similar to that of Fe^{3+} , it is interesting to notice that the $\text{Mn}^{2+}(\text{A}_1)$ electronic states in both models are aligned in the same direction to those of the $\text{Fe}^{3+}(\text{A})$ states. This implies that Mn^{2+} ions assume a similar behaviour to that of the A-site host Fe^{3+} cations. However, unlike those for tetrahedral Fe^{3+} ions, a number of electronic states of the interstitial tetrahedral Mn^{2+} ions (model 2a) align evenly up and down in the valence band. This is further supported by the magnetic moment values attained for these cations to be discussed shortly. For the structure where the extra Mn^{2+} ions occupy interstitial sites (model 2a), the sharp spin-down states (Figure 6), that are related to the Fe^{2+} minority charge at B_{1a} , become localized and slightly shifted away from the Fermi-level, whereas those due to Fe^{2+} at B_4 become less localized as the band becomes broader. This could be ascribed to contributions to the band from the Mn^{2+} ions that have higher energy levels compared to those of $\text{Fe}^{2+}/\text{Fe}^{3+}$ [55]. **For the structural model wherein the extra Mn^{2+} substitute for tetrahedral Fe^{3+} (model 6a), the few states formed at the bottom of the conduction band, which are mainly associated with the empty $\text{Fe}^{3+} t_{2g}$ spin-down states, could imply the reduction of Fe^{3+} at the interstitial and B_3 sites to Fe^{2+} . Alternatively, they could reflect the effect of introducing the Mn^{2+} ions into the Fe_3O_4 structure with their higher energy levels relative to those of the substituted Fe^{3+} [55].**

The values of the hyperfine parameters and magnetic moments, at various cationic positions, calculated for the $1 \times 1 \times 2$ supercell of $\text{Mn}_x\text{Fe}_{3-y}\text{O}_4$ ($y = \frac{2}{3}x$, $x = 0.1$) ($\text{Mn}_3\text{Fe}_{46}\text{O}_{64}$) using the defect model 2a, in which the doped Mn^{2+} ions substitute for tetrahedral Fe^{3+} ions with the extra Mn^{2+} ions occupying interstitial tetrahedral sites, are listed in Table 5. The corresponding values obtained for model 6a, assuming the dopant Mn^{2+} ions to substitute for tetrahedral Fe^{3+} ions and the extra Mn^{2+} ions substituting for a tetrahedral Fe^{3+} , are listed in Table 6. It is clear that, both defect models of $\text{Mn}_x\text{Fe}_{3-y}\text{O}_4$ ($y = \frac{2}{3}x$; ($y = \frac{2}{3}x$, $x = 0.1$)), show, as was reported experimentally [29], that the calculated isomer shift (δ) values at the Fe^{2+} positions decrease whereas those associated with the Fe^{3+} positions increase relative to those of Fe_3O_4 . The general trend of the calculated values of the quadrupole shifts (Δ) obtained using either of the defect models reflects a slightly enhanced symmetry around the Fe nuclei relative to that of the Fe nuclei in Fe_3O_4 . **The small value of the isomer shift (δ) obtained for the interstitial tetrahedral Fe^{3+} is suggestive of shortened bond lengths whereas the relatively large quadrupole shift value is implicative of a distorted environment. The values of both parameters are clearly due to the substitution**

of the Mn²⁺ ions (including the extra ones) for tetrahedral Fe³⁺ ions and the expulsion of the later to interstitial tetrahedral sites (model 6a) [56]. Calculations based on both defect models, show that the effective contact field (B_{hf}) is reduced at all positions when Mn²⁺ is introduced in the structure of Fe₃O₄ supercell as was found experimentally [29]. In general the DFT-calculated hyperfine parameters of Mn_xFe_{3-y}O₄ ($y=2/3x$), based on the most favourable defect structure models proposed by atomistic simulations, vary relative to those of Fe₃O₄ in similar trends to those found experimentally [29].

As is seen from Table 5 and Table 6, both models of the defect **structure yield** calculated Fe magnetic dipole moments, μ_{Fe} , at all investigated sites in the Mn_xFe_{3-y}O₄ ($y=2/3x$); $x=0.1$ supercells that are less relative to the corresponding ones in Fe₃O₄ (Table 4). However, unlike the case of the hyperfine properties, the two models yield contradictory results for the net effective magnetic moment at 0 K (M_0) of Mn_xFe_{3-y}O₄ ($y=2/3x$); $x=0.1$. Our experiments show the net effective magnetic moment (M) of Mn_xFe_{3-y}O₄ ($y=2/3x$); $x=0.1$ nanoparticles to decrease by *ca.* 32%-36% relative to that of Fe₃O₄ as the temperature varies from 5 K to 300 K range [45]. Assuming a modified Bloch's law, fitting the experimental data for the sample with $x=0.1$ has led to an M_0 value of 48.3 emu/g (2.02 μ_B /f.u.) when compared to that of Fe₃O₄ **69.1 emu/g** (2.89 μ_B /f.u.). **We.....**

Low spin values of the Mn²⁺ magnetic moments for (model 2a), where the extra Mn²⁺ ion occupies interstitial tetrahedral sites, are obtained with those at the tetrahedral A₁ sites and the interstitial ones being antiparallel **to the Fe³⁺(A) moments** (Table 5). This leads to a calculated net effective magnetic moment of 4.56 μ_B **that** is higher compared to the calculated one of Fe₃O₄ **because** of the Mn²⁺ spin coupling with the host ions in the sub-lattice. According to Huang *et al* [57], the low spin configuration of the tetrahedral Mn²⁺ ions in a normal spinel ferrite could be referred to the large antiferromagnetic exchange interaction between the Mn²⁺ ions and octahedral Fe³⁺ ones. We assume this is true for **the Mn²⁺ ions** in Mn_xFe_{3-y}O₄ resulting in low spin configuration of Mn²⁺ ions.

In contrast, significant values of the magnetic moment at **the Mn²⁺ ionic** positions are attained for the supercell in (model 6a) (**Table 6**), where all Mn²⁺ ion substitute for Fe³⁺ tetrahedral sites and the expelled Fe³⁺ occupy interstitial sites, compared to those found for (model 2a) . These values are comparable to the Fe³⁺ **magnetic** moment at high spin state, which **are** expected considering the electronic configuration similarity **of the Mn²⁺ and Fe³⁺ cations**. The magnetic

moments of these Mn^{2+} ions are parallel to those in the host sub-lattice whereas the one assigned to the Fe^{3+} at the interstitial site ($\sim 3\mu_B$) is parallel to the Fe^{3+} moments at the A-sites with a B_{hf} value of $\sim 33\text{T}$. The cationic distribution of (model 6a) and the obtained magnetic spin orientation lead to a total ferromagnetic effective moment of $\sim 3.8\mu_B$ which is lower than that calculated for Fe_3O_4 .

It follows from the above computational modeling results that the cationic distribution and behaviour of (model 6a), rather than those of (model 2a), are consistent with the experimental Mössbauer and magnetic trends [29,45].

Conclusion

A study of the Mn^{2+} -doping of Fe_3O_4 where the Mn^{2+} substitute for Fe^{3+} to yield $\text{Mn}_x\text{Fe}_{3-y}\text{O}_4$, ($y = \frac{2}{3}x$) was carried out using atomistic and DFT calculations. Atomistic calculations show the lowest two energy models to be those in which the doped Mn^{2+} ions substitute for Fe^{3+} at the tetrahedral A-sites with either the excess Mn^{2+} ions, required for charge neutrality, or the expelled tetrahedral Fe^{3+} cations occupying interstitial tetrahedral sites. The electronic structure of these two models show ferrimagnetic insulating behaviour ($E_g \sim 0.44\text{ eV}$) for the model wherein Mn^{2+} occupies the interstitial tetrahedral site and half metallic behaviour for the model in which the extra Mn^{2+} substitutes for tetrahedral Fe^{3+} sites with a small variation in the density of states depending on the position of the dopant ions. Overall, it is clear from the electronic structures of these ground state models that the band gap depends strongly on the magnetic ordering and cationic distribution. DFT calculations have shown that the half-metallic $\text{Mn}_x\text{Fe}_{3-y}\text{O}_4$ model leads to variations in the hyperfine and magnetic properties, relative to those Fe_3O_4 , that agree with those obtained experimentally.

Acknowledgement

KSA and HMW acknowledge the support of Sultan Qaboos University (SQU), respectively, for a PhD scholarship and the research grant (SQU/Sci/Phys/04/16). All DFT calculations were carried out using the High-Performance Computing Center of New York University, Abu Dhabi.

References:

- [1] Topsøe, H., Dumesic, J.A., Boudart, M.: *J. DE. Phys.* 12, C6 (1974)
- [2] Sorescu, M., Tarabasanu-Mihaila, D., Diamandescu, L.: *J. Mater. Lett.* 57 (2003) 1867.
- [3] Florea M., Alifanti M., Kuncser V., Macovei D., Apostol N., Granger P., Parvulescu V. I., *J. Catal.*, 316 (2014) 130.
- [4] Kandpal N.D., Sah N., Loshali R., Joshi R., Parasad J., *J. Sci. Ind. Res.*, 73 (2014) 87.
- [5] Widatallah H. M., Berry F. J., Johnson C., M. Pekala, *Solid Stat. Commun.*, 120(2001)171.
- [6] Lyubutin, I.S., Lin, C.R., Yu, V.K., Dmitrieva, T.V., Chiang, R.K.: *J. Appl. Phys.* 106, (2009) 034311.
- [7] Chen, D., Xu, R.: *Mater. Res. Bull.* 33, (1998) 1015.
- [8] Velásquez A.A., Urquijo J.P., *J. SAR.*, 1 (2013) 11.
- [9] Berry F. J., Greaves C., Helgason Ö., MacManus J., *J. Mater. Chem.*, 9 (1999) 223.
- [10] Marand Z.R., Farimani M.H.R., Shahtahmasebi N., *J. Nanomed*, 1 (2004) 238.
- [11] Wang C., Yang S., Chang H., Peng Y., Li J., *J. Mol. Cata. A*, 376 (2013) 13.
- [12] Walz F., *J. Phys: Condensed Matter.*, 14 (2002): R285.
- [13] Jeng H.T., Guo G.Y., Huang D.J., *Phys. Rev. B*, 74 (2006) 195115.
- [14] Attfield J.P., *J. Jpn. Soc. Powder Powder Metallurgy*, 61 (2014) S43.
- [15] Dézsi I., Fetzter Cs., Gombkötő Á., Szűcs I., Gubicza J., Ungár T., *J. Appl. Phys.*, 103 (2008), 104312.
- [16] Verwey E.J.W., *Nature*, 144 (1939) 327.
- [17] Ziese M., *Rep. Prog. Phys.*, 65 (2002) 143.
- [18] Fangw T-T., Chung H.-Y., *J. Am. Ceram. Soc.*, 91 (2008) 342.
- [19] Wright J.P., Attfield J.P., Radaelli P.G., *Phys. Rev. B*, 66 (2002) 214422.
- [20] Wright P., Attfield P., Radaelli P.G., *Phys. Rev. Lett.*, 87 (2001) 266401.
- [21] Schmitz D., Schmitz-Antoniak C., Warland A., Darbandi M., Haldar S., Bhandary S., Eriksson O., Sanyal B., Wende H., *Scientific reports*, 4 (2014) 5760.
- [22] Park S.K., Ishikawa T., Tokura Y., *Phys. Rev. B*, 58 (1998) 3717.
- [23] Kwon W.H., Lee J-G., Choi W.O., Chae K.P., *J. Magn.*, 18 (2013) 26.
- [24] O'Neill H.St.C., Navrotsky A., *American Mineralogist*, 68 (1983) 181.
- [25] O'Neill H.St.C., Dollase W.A., *Phys. Chem. Minerals*, 20 (1994) 541.
- [26] Sorescu M., Mehaila-Tarabasanu D., Diamandescu L., *J. Appl. Phys. Lett.*, 72 (1998) 2047.
- [27] Varsheny D., Yogi A., *Mater. Chem. Phys.*, 128 (2011) 489.
- [28] Taufiq A., Sunaryono, Putra E.G.R., Okazawa A., Watnabe I., Kojima N., Pratapa S., Darminto, *J. Supercond. Nov. Magn.*, 28 (2015) 2855.
- [29] Al-Rashdi K.S., Widatallah H.M., Al Ma'Mari F., Cespedes O., Elzain M., Al-Rawas A.D., Gismelseed A., Yousif A., *Hyperfine Interact.*, 239 (2018) 3.
- [30] Minervini L., Grimes R.W., Tabira Y., Withers R.L., Sickafus K.E., *Philosophical Magazine A*, 82 (2002) 123.
- [31] Moore E. A., *Annu. Rep. Prog. Chem., Sect. A: Inorg. Chem.*, 109 (2013) 421.
- [32] Lewis C. V., Catlow C. R. A., *J. Phys. C: Solid State Phys.*, 18 (1985) 1149.
- [33] Donnerberg H., Catlow C. R. A., *J. Phys.: Condens. Matter*, 5 (1993) 2947.
- [34] Praveen C. S., Timon V., Valant M., *Computat. Mater. Sci.*, 55 (2012) 192.
- [35] Moore E. A., *Annu. Rep. Prog. Chem. A*, 104 (2008) 46.
- [36] Widatallah H., Al-Barwani M.S., Moore E. A., Elzain M., *J. Phys. Chem. Solids*, 119 (2018) 100.
- [37] Lebreau F., Islam M.M., Diawara B., Marcus P., *J. Phys. Chem. C*, 118 (2014) 18133.
- [38] Noura H., *J. Phys. Chem. C*, 76 (2014) 4255.
- [39] Widatallah H., Moore E.A., Babo A.A., Al-Barwani M.S., Elzain M., *Mater. Research Bull.*, 47 (2012) 3995-4000.
- [40] Moore E.A., Bohórquez A., Berry F.J., Helgason Ö., Marco J.F., *J. Phys. Chem. Solids*, 62 (2001) 1277.

- [41] Antonov V.N., Harmon B.N., Yaresko A.N., *Phys. Rev. B*, 67 (2003) 024417.
- [42] Pisani L., Maitra T., Valent' R., *Phys. Rev. B*, 73 (2006) 205204.
- [43] Stoerzinger K.A., Pearce C.I., Droubay T.C., Shutthanandan V., Liu Z., Arenholz E., Rosso K.M., *ACS*, 35 (2019) 13872.
- [44] Assadi M.H.N., Moreno J.J.G, Hanaor D.A.H., Katayama-Yoshida H., *Physical Chemistry Chemical Physics*, 23 (36) (2021) 20129.
- [45] Al-Rashdi K.S., 2018, Physical Properties of Cation-doped and co-doped Binary and Ternary Iron Oxides: Experimental, Atomistic Simulations and First Principle Studies, Ph.D. thesis, Sultanaboos University, Muscat.
- [46] Gale J.D., *J. Chem. Soc., Faraday Trans.*, 93 (1997) 629.
- [47] Moore E.A., Widatallah H.M., *Mater. Res. Bull.*, 43 (2008) 2361.
- [48] Donnerberg H., Catlow C.R.A., *J. Phys.: Condens. Matter*, 5 (1993) 2947.
- [49] Lewis G.V., Catlow C.R.A., Cormack A.N., *J. Phys. Chem. Solids*, 46 (1985) 1227.
- [50] Blaha P., Schwarz K., Madsen G.K.H., Kvasnicka D., Luitz J., Laskowski R., Tran F., Marks L. D., WIEN2k, (Karlheinz Schwarz, Techn. Universitat Wien, Austria), 2018.
- [51] Jeng H.T., Guo G.Y., Huang D.J., *Phys. Rev. Lett.*, 93 (2004) 156403.
- [52] Leonov I., Yaresko A. N., Antonov V. N., Korotin M. A., Anisimov V. I., *Phys. Rev. Lett.*, 93 (2004) 146404.
- [53] Piekarz P., Oleś A.M., Parlinski K., *ACTA Physics Polonica A*, 118 (2010) 307.
- [54] [https://chem.libretexts.org/bookshelves/inorganic_chemistry/modules_and_websites_\(inorganic_chemistry\)/crystal_field_theory/crystal_field_stabilization_energy](https://chem.libretexts.org/bookshelves/inorganic_chemistry/modules_and_websites_(inorganic_chemistry)/crystal_field_theory/crystal_field_stabilization_energy).
- [55] Gauvin-Ndiaye C., Tremblay A.-M. S., Nourafkan R., *Phys. Rev. B*, 99 (2019) 125110.
- [56] Neese F., *Inorganica Chimica Acta*, 337 (2002) 181-192.
- [57] Huang J.-R., Cheng C., *J. Apply. Phys.*, 113 (2013) 033912.

List of Tables:

Table 1: The interatomic potential parameters used to rationalize the defect structure in Mn^{2+} -doped Fe_3O_4 .

Table 2: The calculated defect and lattice energies for $\text{Mn}_x\text{Fe}_{3-y}\text{O}_4$ ($y = \frac{2}{3}x$).

Table 3: Defect energies for the reactions (Table 1) for Mn^{2+} -doped Fe_3O_4 of the composition $\text{Mn}_x\text{Fe}_{3-y}\text{O}_4$ ($y = \frac{2}{3}x$).

Table 4: The calculated isomer shift (δ), quadrupole shift (Δ), the contact hyperfine fields B_{hf} and the magnetic moments μ_{Fe} at various Fe sites in the $1 \times 1 \times 2$ Fe_3O_4 monoclinic supercell.

Table 5: The calculated isomer shift (δ), quadrupole shift (Δ), the contact hyperfine fields B_{hf} and the magnetic moments μ_{Fe} at various Fe sites in the $1 \times 1 \times 2$ $\text{Mn}_x\text{Fe}_{3-y}\text{O}_4$ ($x = 0.1, y = 0.067$) monoclinic supercell with the extra Mn^{2+} ions occupy interstitial tetrahedral sites (model 2).

Table 6: The calculated isomer shift (δ), quadrupole shift (Δ), the contact hyperfine fields B_{hf} and the magnetic moments μ_{Fe} at various Fe sites in the $1 \times 1 \times 2$ $\text{Mn}_x\text{Fe}_{3-y}\text{O}_4$ ($x = 0.1, y = 0.067$) monoclinic supercell with the extra Mn^{2+} ions substituting for tetrahedral Fe^{3+} (model 6).

List of Figures:

Figure 1: The $1 \times 1 \times 2$ supercell of the monoclinic Fe_3O_4 unit cell (see text).

Figure 3: Total DOS obtained from GGA+U calculations of the $1 \times 1 \times 2$ supercell of monoclinic $P2/c$ Fe_3O_4 . The Fermi level is shown by dotted line.

Figure 2: Ions within $2 \times 2 \times 2$ supercell of (a) pure Fe_3O_4 (b) Mn^{2+} -doped Fe_3O_4 with Mn^{2+} ions at tetrahedral sites and the extra Mn^{2+} at interstitial tetrahedral site (Model 2) and (c) Mn^{2+} -doped Fe_3O_4 with Mn^{2+} ions at tetrahedral sites and the Fe^{3+} at interstitial tetrahedral site (Model 6). VESTA 3, Copyright (C) Koichi Momma and Fujio Izumi 2006-2017.

Figure 4: Partial DOS obtained from the GGA+U calculations of the $1 \times 1 \times 2$ supercell of monoclinic $P2/c$ Fe_3O_4 phase. The Fermi level is shown by dotted line. Inside the packets are the corresponding labels of cations positions.

Figure 5: Total DOS obtained from GGA+U calculations for the $1 \times 1 \times 2$ supercell of Mn-doped Fe_3O_4 ($\text{Mn}_x\text{Fe}_{3-y}\text{O}_4, x = 0.1, y = 0.067$) (Model-2). The Fermi level is shown by dotted line.

Figure 6: Partial DOS obtained from GGA+U calculations of the $1 \times 1 \times 2$ supercell of Mn-doped Fe_3O_4 ($\text{Mn}_x\text{Fe}_{3-y}\text{O}_4, x = 0.1, y = 0.067$) (Model-2). The Fermi level is shown by dotted line.

Figure 7: Total DOS obtained from GGA+U calculations of the $1 \times 1 \times 2$ supercell of Mn-doped Fe_3O_4 ($\text{Mn}_x\text{Fe}_{3-y}\text{O}_4, x = 0.1, y = 0.067$) (Model-6). The Fermi level is shown by dotted line.

Figure 8: Partial DOS obtained from GGA+U calculations of the $1 \times 1 \times 2$ supercell of Mn-doped Fe_3O_4 ($\text{Mn}_x\text{Fe}_{3-y}\text{O}_4, x = 0.1, y = 0.067$) (Model-6). The Fermi level is shown by dotted line.

Table 1

Interacting Ions	A (eV)	ρ (Å)	C (eV.Å ⁶)	Spring constant (K/eV.Å ⁻²)	Shell Charge (e)
Fe ³⁺ _{tet} shel -O ²⁻ shel	976.6	0.33	0.0	304.70	4.970
Fe ³⁺ _{oct} shel -O ²⁻ shel	1102.4	0.33	0.0	304.70	4.970
Fe ²⁺ _{oct} shel -O ²⁻ shel	694.1	0.3399	0.0	10.92	2.000
Mn ²⁺ shel -O ²⁻ shel	715.8	0.3464	0.0	81.20	3.000
O ²⁻ shel -O ²⁻ shel	22764.3	0.149	27.88	27.29	-2.207

Table 2

Defect Type/Lattice	Energy (eV)
A tetrahedral Fe ³⁺ vacancy ($V_{Fe_{tet}}'''$)	27.701
An octahedral Fe ³⁺ /Fe ²⁺ vacancy (E_o)	17.899
Oxygen vacancy ($V_{\ddot{O}}$)	11.657
Mn ²⁺ substituting for tetrahedral Fe ³⁺ ($Mn'_{Fe_{tet}}$)	14.603
Mn ²⁺ substituting for octahedral Fe ³⁺ /Fe ²⁺ (E_1)	6.654
Mn ²⁺ at interstitial (A) site (0.125, 0.875, 0.625) ($Mn_{\ddot{int}}$)	-5.417
Mn ²⁺ at interstitial (B) site (0.250, 0.250, 0.000) ($Mn_{\ddot{int}}$)	-5.996
Fe ²⁺ as dopant substituting for octahedral Fe ³⁺ /Fe ²⁺ (E_2)	5.994
Fe ³⁺ as dopant substituting for octahedral Fe ³⁺ /Fe ²⁺ (E_3)	-7.081
Fe _A ³⁺ at interstitial (A) site (0.125 0.875 625) ($Fe_{\ddot{int}}$)	-19.369
Fe _A ³⁺ at interstitial (B) site (0.250 0.250 0.000) ($Fe_{\ddot{int}}$)	-19.713
Fe _B ³⁺ at interstitial (A) site (0.125 0.875 625) ($Fe_{\ddot{int}}$)	-17.638
Fe _B ³⁺ at interstitial (B) site (0.250 0.250 0.000) ($Fe_{\ddot{int}}$)	-18.466
$Mn_{Fe_{oct}}^{(0.5)'} = E_1 - E_3 = 6.654 + 7.081$	13.735
$Fe_{Fe_{oct}}^{(0.5)'} = E_2 - E_3 = 5.994 + 7.081$	13.075
$V_{Fe_{oct}}^{(2.5)'} = E_o - E_3 = 17.899 + 7.081$	24.980
$Fe_{Fe_{oct}}^{(0.5)_{3+}} = E_3 - E_2 = -7.081 - 5.994$	-13.075
MnO	-38.380
α -Fe ₂ O ₃	-149.236

Table 3

Defect Reaction	Process	Defect Energy (eV)
1a	Two-third of a B-site Fe ³⁺ is substituted by Mn ²⁺ balanced by occupation of one-third of Mn ²⁺ in an interstitial (A) site	4.70233
1b	Two-third of a B-site Fe ³⁺ is substituted by Mn ²⁺ balanced by occupation of one-third of Mn ²⁺ in an interstitial (B) site	-0.21067
2a	Two-third of an A-site Fe ³⁺ is substituted by Mn ²⁺ balanced by occupation of one-third of Mn ²⁺ in interstitial (A) site	-3.43567
2b	Two-third of an A-site Fe ³⁺ is substituted by Mn ²⁺ balanced by occupation of one-third of Mn ²⁺ in interstitial (B) site	-3.62867
3	Mn ²⁺ occupies an interstitial (A) site balanced by 2/3 vacancy in an B-site Fe ³⁺	8.58767
4	Mn ²⁺ occupies an interstitial (A) site balanced by 2/3 vacancy in an A-site Fe ³⁺	1.6850
5a	Mn ²⁺ substitutes for a B-site Fe ³⁺ balanced by expulsion of 1/3 of Fe ³⁺ from the B-site to an interstitial (A) site	9.56533
5b	Mn ²⁺ substitutes for a B-site Fe ³⁺ balanced by expulsion of 1/3 of Fe ³⁺ from the B-site to an interstitial (B) site	9.28933
6a	Mn ²⁺ substitutes for an A-site Fe ³⁺ balanced by expulsion of 1/3 of Fe ³⁺ from the A-site to an interstitial A-site	-3.21867
6b	Mn ²⁺ substitutes for an A-site Fe ³⁺ balanced by expulsion of 1/3 of Fe ³⁺ from the A-site to an interstitial B-site	-3.33333
7a	Two-third of an A-site Fe ³⁺ is substituted by Mn ²⁺ and one-third of a B-site Fe ³⁺ is substituted by Mn ²⁺ balanced by expulsion of 1/3 of Fe ³⁺ from the B-site to an interstitial (A) site	1.42733
7b	Two-third of an A-site Fe ³⁺ is substituted by Mn ²⁺ and one-third of a B-site Fe ³⁺ is substituted by Mn ²⁺ balanced by expulsion of 1/3 of Fe ³⁺ from the B-site to an interstitial (B) site	1.15133
8a	Two-third of an A-site Fe ³⁺ is substituted by Mn ²⁺ and one-third of a B-site Fe ³⁺ is substituted by Mn ²⁺ balanced by expulsion of 1/3 of Fe ³⁺ from the A-site to an interstitial (A) site	0.85033
8b	Two-third of an A-site Fe ³⁺ is substituted by Mn ²⁺ and one-third of a B-site Fe ³⁺ is substituted by Mn ²⁺ balanced by expulsion of 1/3 of Fe ³⁺ from the A-site to an interstitial (B) site	0.73567

Table 3: (continued)

Defect Reaction	Process	Defect Energy (eV)
9a	Two-third of a B-site Fe^{3+} is substituted by Mn^{2+} and one-third of an A-site Fe^{3+} is substituted by Mn^{2+} balanced by expulsion of 1/3 of Fe^{3+} from the A-site to an interstitial (A) site	4.91933
9b	Two-third of a B-site Fe^{3+} is substituted by Mn^{2+} and one-third of an A-site Fe^{3+} is substituted by Mn^{2+} balanced by expulsion of 1/3 of Fe^{3+} from the A-site to an interstitial (B) site	4.80467
10a	Two-third of a B-site Fe^{3+} is substituted by Mn^{2+} and one-third of an A-site Fe^{3+} is substituted by Mn^{2+} balanced by expulsion of 1/3 of Fe^{3+} from the B-site to an interstitial (A) site	5.49633
10b	Two-third of a B-site Fe^{3+} is substituted by Mn^{2+} and one-third of an A-site Fe^{3+} is substituted by Mn^{2+} balanced by expulsion of 1/3 of Fe^{3+} from the B-site to an interstitial (B) site	5.22033

Table 4

Ion (position #)	$\delta/$ (mm/s)	$\Delta/$ (mm/s)	$B_{hf}/$ (T)	$\mu_{\text{Fe}}/(\mu_B)$
Fe^{2+} (B_{1a})	0.895	1.173	-33.59	3.53
Fe^{2+} (B_4)	0.928	1.639	-32.08	3.50
Fe^{3+} (A_1)	0.148	-0.142	37.23	-4.09
Fe^{3+} (A_1)	0.150	-0.142	37.35	-4.09
Fe^{3+} (A_1)	0.152	-0.142	37.55	-4.09
Fe^{3+} (A_1)	0.150	-0.143	37.27	-4.09
Fe^{3+} (A_2)	0.140	-0.234	37.62	-4.09
Fe^{3+} (B_{2a})	0.280	-0.168	-37.69	4.20
Fe^{3+} (B_3)	0.317	0.177	-38.88	4.16

Table 5

Ion (position #)	$\delta/$ (mm/s)	$\Delta/$ (mm/s)	$B_{hf}/$ (T)	$\mu_{Fe}/(\mu_B)$
Fe ²⁺ (B _{1a})	0.870	1.114	-33.35	3.40
Fe ²⁺ (B ₄)	0.905	1.351	-32.67	3.36
Fe ³⁺ (A ₁)	0.152	-0.150	36.27	-3.93
Mn ²⁺ (A ₁)	-----	-----	-----	0.09
Mn ²⁺ (A _{int})	-----	-----	-----	1.04
Mn ²⁺ (A ₁)	-----	-----	-----	-0.66
Fe ³⁺ (A ₂)	0.146	-0.227	36.89	-3.92
Fe ³⁺ (B _{2a})	0.286	-0.163	-36.32	4.05
Fe ³⁺ (B ₃)	0.357	0.207	-34.96	3.97

Table 6

Ion (position #)	$\delta/$ (mm/s)	$\Delta/$ (mm/s)	$B_{hf}/$ (T)	$\mu_{Fe}/(\mu_B)$
Fe ²⁺ (B _{1a})	0.855	1.078	-33.43	3.39
Fe ²⁺ (B ₄)	0.890	1.609	-30.76	3.35
Fe ³⁺ (A ₁)	0.151	-0.128	36.32	-3.91
Mn ²⁺ (A ₁)	-----	-----	-----	-4.07
Fe ³⁺ (A _{int})	0.007	-1.187	33.09	-2.91
Mn ²⁺ (A ₁)	-----	-----	-----	-4.07
Fe ³⁺ (A ₂)	0.144	-0.228	36.99	-3.90
Fe ³⁺ (B _{2a})	0.286	-0.164	-35.95	4.02
Fe ³⁺ (B ₃)	0.334	-0.132	-36.94	3.97